Waste chicken bone-derived porous carbon materials as high performance electrode for supercapacitor applications

Delvina Japhet Tarimo, Kabir O. Oyedotun, Ndeye Fatou Sylla, Abdulmajid A. Mirghni, Ndeye Maty Ndiaye and Ncholu Manyala*.

Department of Physics, Institute of Applied Materials, SARChI Chair in Carbon Technology and Materials, University of Pretoria, Pretoria 0028, South Africa.

*Corresponding author's email: ncholu.manyala@up.ac.za, Tel.: + (27)12 420 3549.

HIGHLIGHTS

- Animal bone waste (CCBW) was successfully converted into activated carbon.
- The optimal KOH to CCBW ratio (1:1) presented the highest specific capacitance.
- The CCBW-1 was used as a positive and negative electrode in the symmetric device.
- The fabricated device proves great potential for supercapacitors applications.

ABSTRACT

Cooked chicken bone waste (CCBW) has been traditionally used as the source of food for some animals like dogs in developing countries, all the same, it has never been reported as an energy storage material. In this study, CCBW has been successfully converted into carbon materials (activated carbon) through a simple and cost-effective activation process for supercapacitor applications. The influence of potassium hydroxide (KOH) as an activating agent/CCBW ratio was established by different characterization techniques and electrochemical investigation. The synthesized activated carbon with the optimal KOH to CCBW presented a high specific capacitance with the specific surface area of 2235.8 m^2/g. The fabricated symmetric device presented a maximum specific energy and power of 17.1 Wh kg^{-1} and 425 W kg^{-1} at 0.5 A g^{-1}. Besides, at high specific current of 10 A g^{-1} the device was able to maintain a specific energy and power of 11.3 Wh kg^{-1} and 8500 W kg^{-1}, respectively. The device established a remarkable

columbic efficiency of 99.8% and capacitance retention of 90.1% after 20,000 cycling at 5 A g^{-1}. An outstanding improvement in specific capacitance from 127.6 F g^{-1} to 329.41 F g^{-1} after the device was subjected to floating time of 300 h was noted, with corresponding specific energy and power of 33.1 Wh kg^{-1} and 4,250 W kg^{-1} at 5 A g^{-1}. The results attained offers a possible process of transforming low-cost distinguished biomass source into highly porous nanostructured constituents for energy-storage applications.

GRAPHICAL ABSTRACT

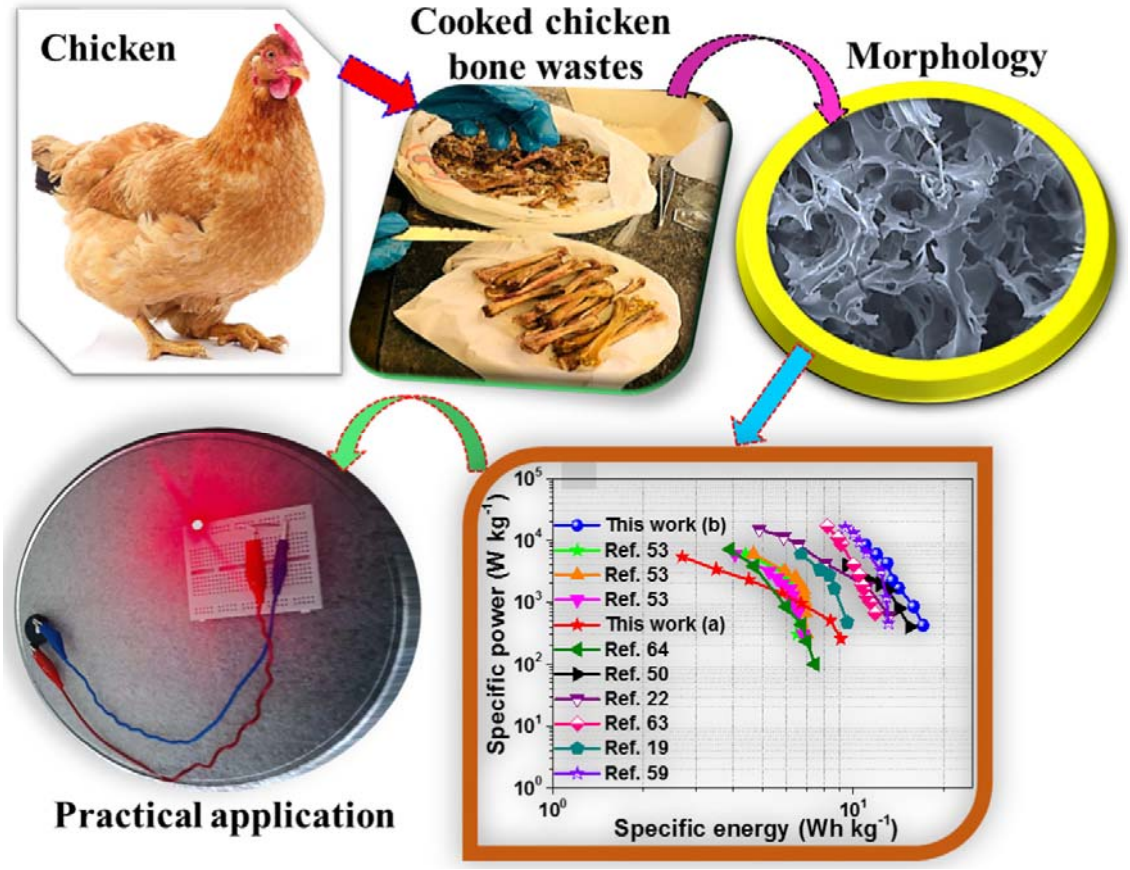

KEYWORDS: Cooked chicken bone waste; Biomass; Activated carbon; Carbonization, Specific surface area, Energy storage.

1. INTRODUCTION

The rapid consumption of fossil fuel which occur as a result of economic growth is depleted and it also cause health problems from the greenhouse gas emission. This calls for the global concern about the health of our society, ecological unit and sustainable future development [1–4]. Besides, the United Nations General Assembly (2015) in the Sustainable Development Goals (SDGs) number 7 "Affordable and Clean Energy" emphases on evolving in solar, wind and thermal power aiming at safeguarding and improving energy efficiency for all through expanding infrastructure and upgrading technology so as to afford clean and efficient energy in all countries which will reassure the development and help the environments [5]. The further investigation on the expansion and scale up of the sustainable clean energy sources and their associated technologies is of paramount. On the other hand, there is limitation on the full utilization of renewable clean energy sources due to climate change which demands enlargement of energy linked conversion system and storage devices to efficiently harvest these periodic energy sources [6,7].

Furthermore, the growth in the energy demand provides an alternative means of producing energy in surplus. However, the energy produced requires energy storage devices which can accommodate the produced energy and being used when needed [8,9]. Batteries, supercapacitors and fuel cells are examples of the energy storage/conversion devices [10]. Batteries (traditional energy storage) with massive weight and larger volume have been employed as the electrochemical energy storage devices due to their capability to deliver high specific energy. However, toxicity, high maintenance cost, rapid capacity reduction, low specific power and short life span remain as their weaknesses particularly, in the application demanding high instantaneous power like elevators, airplane emergency doors, and engine car start. Also, the development of high-performance devices like electric vehicles, portable

electronic devices and smart grid remain as the main need for an alternative power resources than the traditional energy resources [10–14].

As a result, supercapacitors have been considered as a supplement for traditional energy storage like battery or in hybrid with batteries as means to answer the request to alternative clean energy because of its unique properties like high cycle life, low maintenance cost, easy portability, light weight, and high specific power as compared to batteries. The fundamental challenge limiting the large scale commercialization of supercapacitor is the small specific energy delivered when fully charged [15,16]. Since the specific energy is proportional to the specific capacitance and the square of the voltage, thus increasing these two parameters are beneficial for increasing specific energy [17–19]. This can be undertaken by developing a cost effective and environmentally friendly novel electrode material of much improved capacitance, optimization of structure in the combined system and electrolytes having wider operating potential. For example, synthesis of new electrode material should take into account the compatibility between the size of the electrolyte ions with the size of the pore structure of the material so as to produce electrode material with high specific capacitance [7,20–23]. On the other hand, good electrolyte has good electrochemical stability, small solvated ion radius, broader range of operating temperature, high conductivity, low cost, environmentally friendly and wider operating potential [24–26]. In addition, some studies have suggested the use of new reference electrode such as ZnO/Zn or HgO/Hg as means to answer the limitation of low specific energy of supercapacitors through maximizing the full working voltage of the electrode material [27,28].

Supercapacitors (SC) can be prepared by using carbonaceous material (e.g. activated carbon-AC, carbon nanotubes-CNT, carbon aerogel, graphene), conducting polymer (e.g. PANI,

PEDOT) and transition metal oxides/hydroxides (e.g. CoO, NiO, NiOH, MnO_2) [29–35]. However, SC performance is influenced by high specific capacitance which results from high specific surface area (SSA) of the material and stability of the electrolytes [24,36–38]. In contrast with other materials AC offers exceptional power density, longer cycling and high specific surface area (SSA) which enhances the active sites of the material consequently allowing easy accessibility of ions from the electrolyte. Also, due to their eco-friendly nature and low cost of production, AC has been well-thought-out as the preeminent topnotch for producing SC [39–41].

Conventionally, mostly AC was synthesized from coal, petroleum and their derivatives which are depleting and have environmental pollutions like greenhouse effect and human health's problems [42]. This conveyed attention to the investigators to explore sustainable and renewable resources waste as the potential basis for producing AC. The choice of these wastes is determined by availability of the material for cost-effectiveness, low degradation rate upon storage, high carbon content, high yield content and small content of inorganic material so as to reduce the possibility of ash formation [43–46]. Some of these wastes include animal waste and plant waste whereby when utilized for SC it will reduce material wastage, enhance application of natural resources and conserve the environment.

Cooked chicken bone waste (CCBW) from animal waste has been traditionally thrown away as biomass wastes. In some places it has been used as the source of food for some animals like dogs especially in the developing countries. All the same, and to the best of our knowledge it has never been reported as the energy storage material. In this study we are reporting for the first time the use of CCBW waste as the source of novel electrode material for SC applications. In addition, different literature reported the synthesis of new AC for SC from plant wastes

[3,47–51]. Only few studies have reported the synthesis of AC from animal wastes specifically bone waste for SC applications [16,52,53]. On the other hand, comparisons of electrolytes on the stated few studies is deficient as mostly use acidic and ionic electrolyte which is expensive and not environmentally friendly.

Herein, the CCBW has been successfully converted into carbon material (activated carbon) through a simple and cost-effective activation process for SC applications. The activated carbon was synthesized by a modified activation method, where the pre-eminent temperature of the carbonized CCBW was determined followed by treatment with KOH as activating agent at different ratios. The best performance was noted for KOH:CCBW ratio 1:1 (CCBW-1) carbonized at 700 ^{o}C with the highest specific surface area of 2235.8 m^2/g. For performance comparison, the electrochemical analysis of the CCBW was evaluated in aqueous basic (3 M KOH) electrolyte and different neutral (1 M Li_2SO_4, 1 M $NaNO_3$, 1 M Na_2SO_4 and 2.5 M KNO_3) electrolytes. The optimum performance was noted for 1 M $NaNO_3$ electrolyte in a positive and negative potential window of 0.0 – 0.7 V vs Ag/AgCl and -0.9 – 0.0 V vs Ag/AgCl, respectively. The fabricated symmetric device presented a maximum specific energy and power of 17.1 Wh kg^{-1} and 425 W kg^{-1} at 0.5 A g^{-1}, respectively. A significant columbic efficiency of 99.8% and capacitance retention of 90.1% was recorded after 20,000 cycling at 5 A g^{-1}. An exceptional increase in specific capacitance from 127.6 F g^{-1} to 329.41 F g^{-1} after the device was exposed to floating time of 300 h was noted, with equivalent specific energy and power of 33.1 Wh kg^{-1} and 4,250 W kg^{-1} at 5 A g^{-1}. The achieved results suggest a promising progress of converting economical and notorious CCBW source into substantially porous nanostructured materials for energy-storage applications.

2. EXPERIMENTAL DETAILS

2.1 Material synthesis

The activated carbon from cooked chicken bone waste (CCBW) was produced as follows: The CCBW type of broiler was collected after eating chicken during the COVID-19 lockdown (April-June, 2020) in Pretoria, South Africa. The CCBW was cleaned with ethanol and then dried in the oven for 24 h at 60 ^{o}C. 5 g of the dried bones were pre-carbonized at 400 ^{o}C for 4 h using argon gas (200 sccm in a flow rate of 5 ^{o}C/min) to remove volatile particles and impurities. Thereafter, the pre-carbonized material was mixed with potassium hydroxide (weight ratio of 1:1) as activating agent in the agitate motor followed by addition of few drops of water to form a compact block like structure which was dried in the oven at 100 ^{o}C for 12 h. Thereafter, the mixture was carbonized at 600, 700 and 800 ^{o}C for 2 h under argon environment (300 sccm at 5 ^{o}C/min) to obtain the suitable temperature (figure S1). The attained sample was soaked in 3 M HCl, which was intended to further remove dissolved organic impurities as well as neutralising the remaining activating agent in the samples, and later washed thoroughly with deionized water until neutral pH is obtained. The obtained sample was dried in the oven at 60 ^{o}C for 24 h. Afterwards, the carbonization process was repeated by mixing the pre-carbonized CCBW with KOH at different ratios using 700 ^{o}C as the best carbonization temperature for good electrochemical performance and the obtained samples were named as CCBW-0.5, CCBW-1 and CCBW-2 indicating a mass ratio of 1:0.5, 1-1 and 1-2, respectively (Scheme 1).

Scheme 1: Schematic demonstration for the synthesis of cooked chicken bone waste (CCBW).

2.2 Material characterization

Material characterizations were completed through the following techniques: Scanning electron microscope (Field Emission Scanning Electron Microscope (FE-SEM); SEM-Zeiss Ultra plus 55; Akishima-shi, Japan) fitted out with an energy-dispersive spectroscopy (EDS) was employed to analyse the surface morphology and elemental analysis of the synthesized CCBW samples. Imaging was done In Lens under high vacuum through acceleration voltage of 2.0 kV. The high-resolution transmission electron micrographs were completed by HRTEM FEI Tecnai-F30; Akishima-shi, Japan functioned at 1.0 kV. NOVATOUCH built-in with a quanta-chrome Touch-Win software was utilized to study the Nitrogen adsorption-desorption isotherms. High vacuum environment was applied to degas the sample for 12 hours at 150 ^{o}C. The SSA was evaluated from the adsorption branch via Brunauer-Emmett-Teller (BET) technique in the relative pressure range (P/Po) of 0.01-0.2. The pore size distribution was calculated from the desorption isotherms via a density function theory (DFT) software which part of the equipment analysis system. A WITec alpha 300 RAS+ Confocal micro-Raman microscope operated at 5 mW, 150 s and 532 nm for laser power, spectral acquisition time and laser wavelength, respectively. X-ray diffraction (XRD - Bruker BV 2D PHASER Best

Benchtop; PANalytical BV, Amsterdam, Netherland) operated with a Cu K_{α_1} radiation source ($\lambda = 0.15406\ nm$) at 30 mA and 50 kV was used to study the phase structures of the CCBW samples in reflection geometry at 2θ values (5 - 90^o) in a step size of 0.005^o.

2.3 Electrochemical characterization

The electrochemical evaluation of the CCBW samples was investigated using three- and two-electrode configurations with the aid of a Bio-Logic VMP300 potentiostat (Knoxville TN, USA) run using the EC-Lab VI.41 software. The mixture consists of CCBW sample (working material; 80 %), conductive carbon acetylene (CAB; 10 %) and polyvinylidene (PVDF – binder; 10 %) was used to prepare electrodes by adding few drops of 1-methyl 2-pyrollidone (NMP) to make a slurry. The slurry was coated onto a nickel foam, 1.0 x 1.0 cm^2 and thickness-diameter of 0.2 by 16 mm acting as a current collector for three- and two-electrode, respectively, subsequently drying in the oven at 60 ^{o}C for 12 h. For three-electrode evaluation; Ag/AgCl was used as a reference electrode, glassy carbon as a counter electrode, and CCBW sample as a working electrode. For two-electrode evaluation a Watman Celgard paper-based separator was employed in a standard 2032 grade coin cell. Measurements were established via cyclic voltammetry (CV), galvanostatic charge discharge (GCD) and electrochemical impedance spectroscopy (EIS).

3. RESULTS AND DISCUSSION

3.1 Microstructure analysis of CCBW

Figure 1 (a, b), (d, e) and (h, i) displays the SEM morphology for CCBW-0.5, CCBW-1 and CCBW-2 samples at low and high magnification, respectively while (c, f, j) indicates their matching TEM micrographs. All samples display cavity framework with interconnecting

irregular shaped cavities which results from elimination of unstable composites throughout carbonization. These cavities are attributed to the collaboration between potassium hydroxide (KOH) used as an activating agent and the raw material (CCBW) used as a source of carbon. In this process, the decomposition of KOH generates potassium bicarbonate, potassium metallic and hydrogen gas ($6KOH + 2C \leftrightarrow 2K + 3H_2 + 2K_2CO_3$) whereby at a temperature of 700 ^oC or greater the decomposition of potassium bicarbonate produces carbon monoxide (CO) and carbondioxide (CO_2) gases which promotes further pore activation through carbon gasification [49,54]. This confirm polymerization reaction that occur between the raw material and activating agent during carbonization in which the carbon structure is scratched to create pores through oxidation of carbon into carbonate ions. Furthermore, the generated potassium metallic broadens the spaces between the carbon atomic layers during intercalation thus increases SSA and pore volume which later detached throughout the washing process. There was no significant difference in the morphology despite the variation of activating agent ratio, however this type of porous structure can be effectively used for SC storage applications.

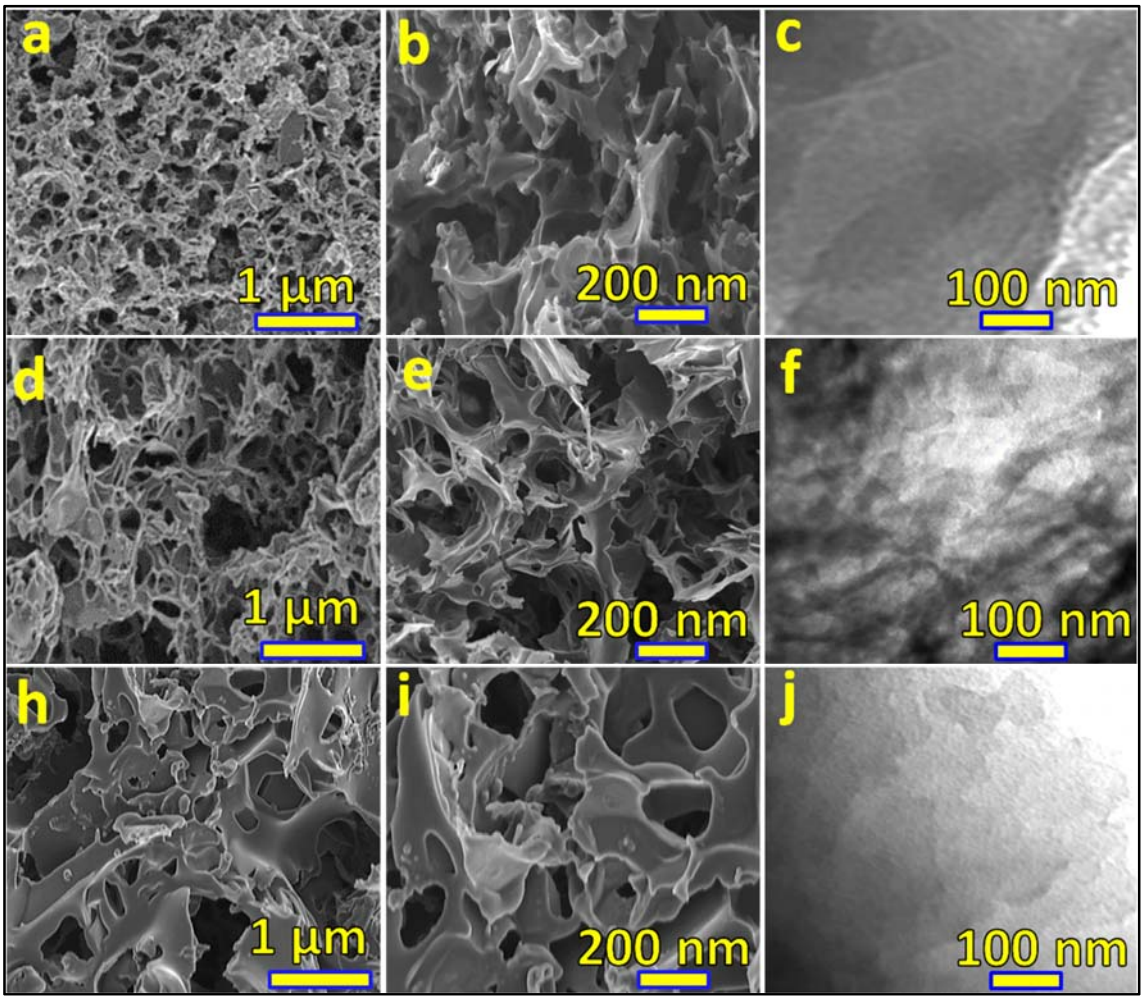

Fig. 1: (a, b), (d, e) and (h, i) are SEM images of CCBW-0.5, CCBW-1 and CCBW-2 at low and high magnifications, respectively. (c, f and j) are TEM images of CCBW-0.5, CCBW-1 and CCBW-2, respectively.

Figure 2 (a, b and c) shows the EDS measurements of the samples indicating the elemental mapping and composition of CCBW-0.5, CCBW-1 and CCBW-2, respectively. The results established the distribution of carbon (C), oxygen (O) and small content of sulphur (S) within the materials. The observed S spot is one of the elements in chicken bone which was not removed completely during pre-carbonization, carbonization and washing processes and hence is expected to act as general doping element to enhance the specific capacitance. Figure 2 (b; CCBW-1) display high density of carbon compared to figure 2 (a; CCBW-0.5 and c; CCBW-

2) which confirms high porous structure within this particular sample and is expected to contribute in the electrochemical performance.

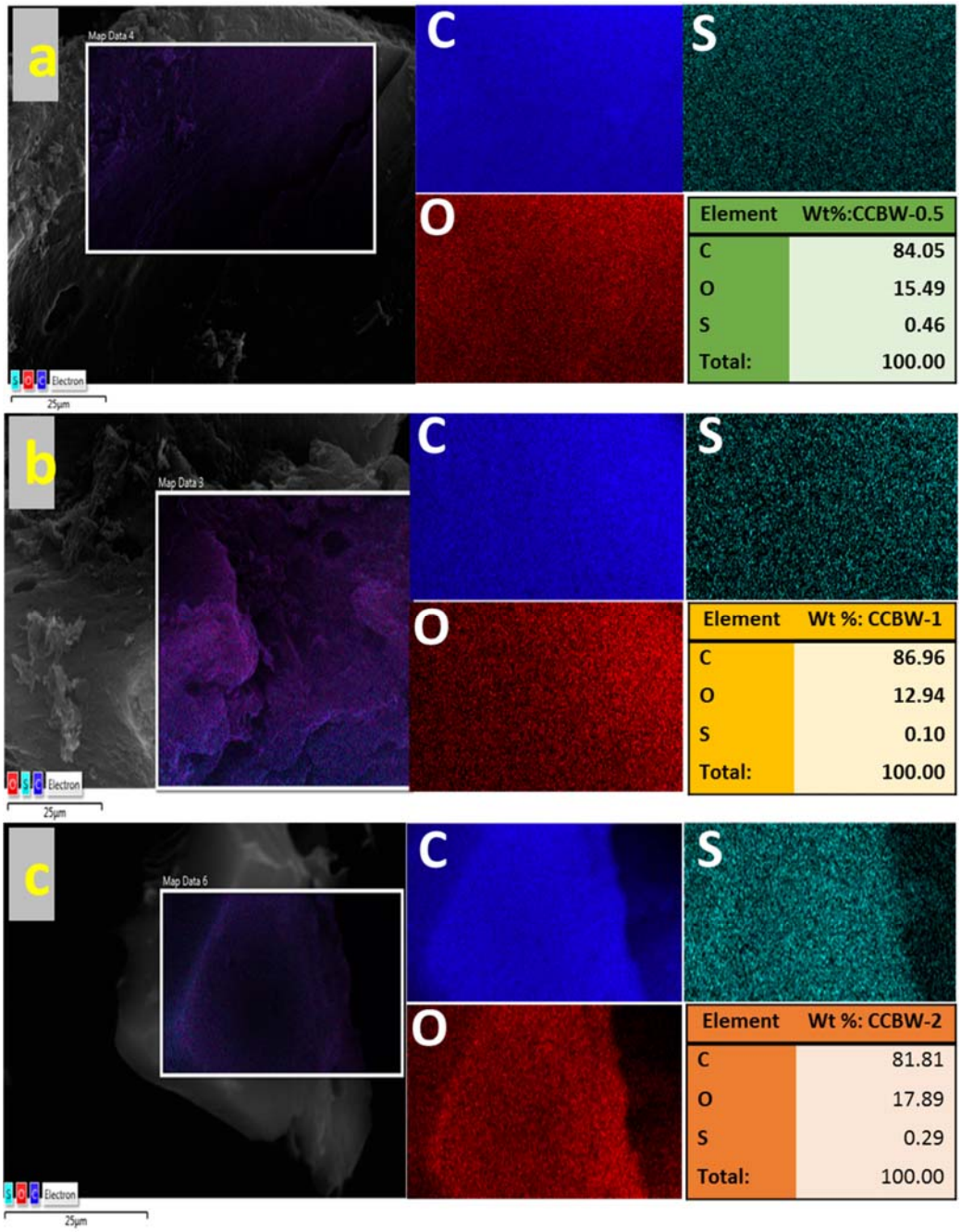

Fig. 2: Illustrates the elemental mapping of carbon (C), oxygen (O), sulphur (S) and their corresponding EDS of (a) CCBW-0.5, (b) CCBW-1 and (c) CCBW-2, respectively.

3.2 BET specific surface area analysis of CCBW

Figure 3 (a) displays the N_2 adsorption/desorption curve for the CCBW-0.5, CCBW-1 and CCBW-2 samples in which CCBW-0.5 ratio displays type III and H3 hysteresis loop while CCBW-1 and CCBW-2 display type II isotherms and H4 hysteresis loop. The evaluated BET specific surface areas (SSAs) were 1617.4, 2235.8 and 1245.4 m^2/g for CCBW-0.5, CCBW-1 and CCBW-2, respectively. The lowest SSA in CCBW-0.5 could be attributed to the lower degree of activation due to insufficient amount of KOH activating agent used. The highest SSA is observed for CCBW-1 which is an indication of an efficient consumptions of KOH in the raw materials which reveal that 1-1 is the right amount for the KOH and the raw materials to interact with each other and is expected to influence the electrochemical performance. This is because an increase in SSA of CCBW-1 is anticipated to escalate more electrochemical active sites within the electrode. Thus, facilitates the contact between the ions in the electrolyte and the active material which reduce diffusion resistance and increase the specific capacitance. The SSA value (2235.8 m^2/g) for CCBW-1 is higher and comparable to cattle bone (2096 m^2/g) [55], bovine bone (1383 m^2/g) [16], pig bone (2157 m^2/g) [52], pork bone, blackfish and Eel bone (1260, 1202 and 1163 m^2/g) [53], which are the few reported AC from animal bones for SC applications. The reduction in SSA for CCBW-2 categorize the saturation reaction process which occur due to the disproportionate amount of KOH activating agent in which sometimes remain unreacted and hence prevent the formation of additional pores after a certain limit. Fig 3 (b) shows the pore size distribution for all samples with a peak between 0.83 and 5.6 nm showing the distribution of micropores and mesopores within the materials. Micropores support the charge-storage mechanism while mesopores facilitate the successful transfer of ions from the electrolytes thus increase the electrochemical performance of a SC.

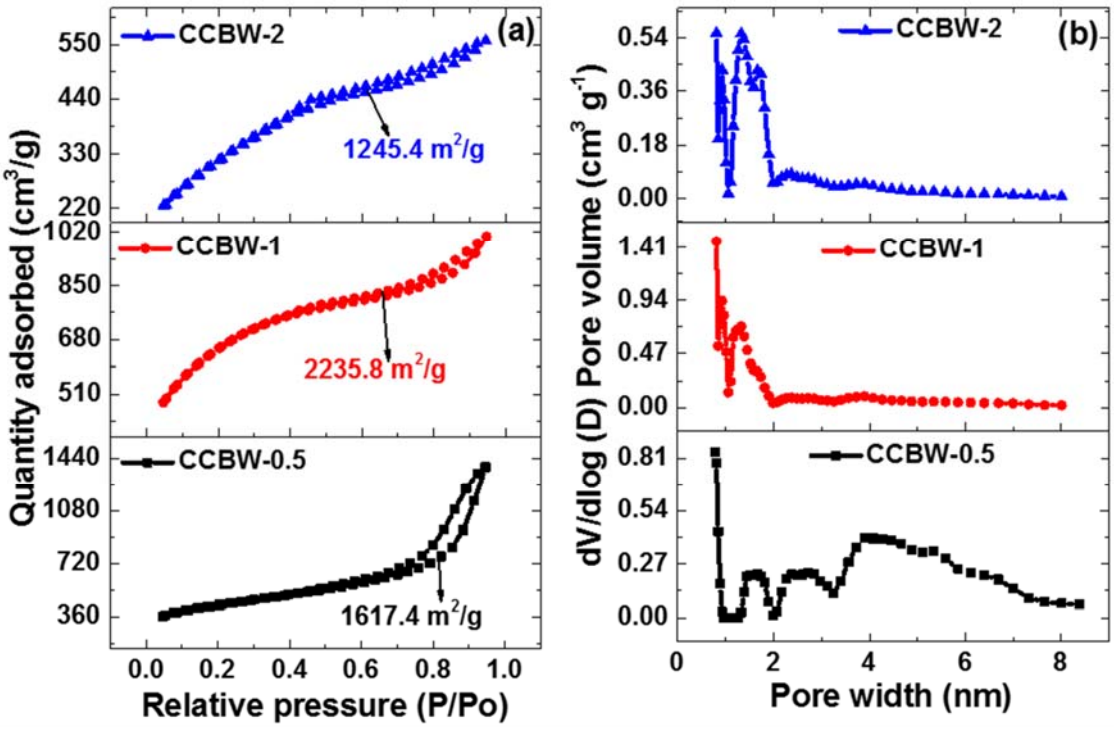

Fig. 3: (a, b) N_2 absorption-desorption isotherms and pore size distribution of CCBW-0.5, CCBW-1 and CCBW-2, respectively.

3.3 Structural properties (Raman and XRD) analysis of CCBW

The Raman and XRD analysis were implemented to study the structural properties of the synthesized materials. The Raman spectra for all samples are represented in figure 4 (a) displaying the presence of D, G and 2D bands [50,51,56]. The characteristic peak of the D band around 1345 cm^{-1} is associated with defects in the carbon matrix which occur when the carbon atoms appear at the edge planes is perpendicular to the single carbon sheets of the bulk graphitic materials. The G band at 1596 cm^{-1} is a characteristic of sp^2 hybridized carbon which rises from the stretching of C-C bond in the graphitic material. The existence of 2D at 2855 cm^{-1} is due to the second order phonon which distinguish number layers of carbon materials. The degree of defects was estimated by I_d/I_g ratio showing the CCBW-0.5 and CCBW-2 having 0.85 and 0.83, respectively while the CCBW-1 has an estimation of 0.99 approximately 1 revealing good

interaction between KOH and CCBW thus present the enhancement of disorder or defect structure for this activated carbon. It was further observed that D, G and 2D band were able to maintain the same position regardless of the KOH variation however the 2D band of CCBW-1 has reduced significantly compared to CCBW-0.5 and CCBW-2 presenting good contact between KOH and the raw material since this band is very sensitive to defects.

XRD study is the distinguished description for identification of crystallinity/amorphous nature of the carbon layers prevailing in the synthesised material. The XRD spectrum of the produced materials is presented in figure 4 (b) whereby all three samples confirm the occurrence of three broad peaks at 2θ around 10.2°, 30.1° and 42.0° corresponding to (001), (220) and (100) crystal plane of carbon materials (JCPDS 00-056-0159) [57]. The trivial peak shift from lower degree of 10.2° for CCBW-1 with its amorphous structure indicates the presence of defect structure required for electrochemical performance. The broadness of the peaks reveals the presence of porous carbon with low crystallinity signifying that the raw material has been efficiently transformed into amorphous carbon.

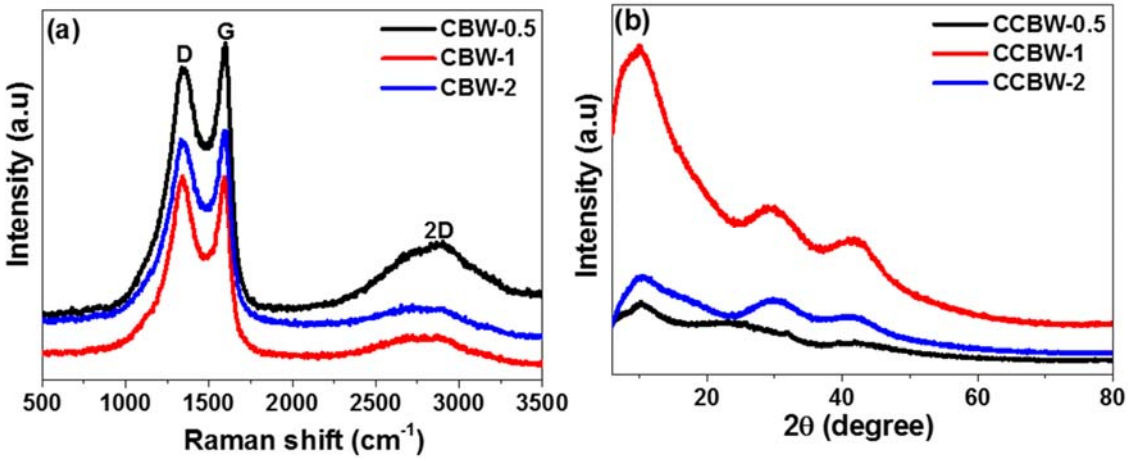

Fig. 4: (a) Raman and (b) XRD spectrum of CCBW-0.5, CCBW-1 and CCBW-2, respectively.

3.4 Electrochemical exploration of CCBW

3.4.1 Three-electrode evaluation

To assess the operational condition of the synthesized samples, the electrochemical behavior was performed in a three-electrode configuration using mass electrode of 3.0 mg/cm^2 and 3 M KOH basic aqueous electrolyte so as to confirm the notable carbonizing temperature for CCBW in a weight ratio of 1-1. Figure S1 (a, b and c) show the cyclic voltammetry (CV) curves at 50 mV s^{-1}, galvanostatic charge-discharge (GCD) curves at 1 A g^{-1} and EIS Nyquist plot for CCBW at 600 ^{o}C, 700 ^{o}C and 800 ^{o}C, respectively in a higher negative potential range -1.05 – 0 V vs Ag/AgCl. The CV curves displayed the rectangular shape while the GCD curves displayed the triangular shape revealing the EDLC behaviour. From the figure, it can be witnessed that the sample carbonized at 700 ^{o}C has high current response in the CV curve, longer discharge time in the GCD curve and shorter diffusion length in the EIS Nyquist plot revealing to be the right carbonization temperature for good electrochemical performance as compared to 600 ^{o}C and 800 ^{o}C carbonization temperatures. The analysis of the material in the negative potential window confirms the EDLC behavior as the characteristics of the carbon materials. The positive potential window displayed the Faradic behavior (figure S2 (a)) which limits the properties of capacitive material and hence more attention was paid to the negative potential window for this particular electrolyte (3 M KOH). From these results 700 ^{o}C was selected for further sample preparation through variations of activating agent (KOH) ratio to raw material and then electrochemical measurements were analysed.

Figure 5 (a, b, c and d) illustrates the CV curves at 50 mV s^{-1}, GCD curves at 1 A g^{-1}, specific capacitance versus specific current at different specific currents and EIS Nyquist plot for CCBW-0.5, CCBW-1 and CCBW-2 at 700 ^{o}C, respectively, presenting the variation of mass ratio between the raw material (CCBW) and the activating agent (KOH). The same operating

potential window (-1.05 – 0 V vs Ag/AgCl) and the EDLC behaviour was maintained by all samples regardless of the variation of the mass ratio between CCBW and KOH. The 1:1 mass ratio (CCBW-1) demonstrates high current response in the CV curve (figure 5 (a)), longer discharge time in the GCD curve (figure 5 (b)), high specific capacitance (figure 5 (c)) and shorter diffusion length in the EIS Nyquist plot (figure 5 (d)) revealing higher electrochemical performance compared to CCBW-0.5 and CCBW-2 samples. The GCD profile was employed to evaluate the specific capacitance (C_s) of the CCBW through the following equation [9]:

$$C_s = \frac{I_d \times \Delta t}{m \times \Delta V} \text{ [F g}^{-1}\text{]} \quad (1)$$

where, I_d presents discharge current in (mA), ΔV stands for operating potential window in (V), Δt (s) represents electrode discharge time, and m is the mass loading of the active material in (mg).

The highest specific capacitances recorded for CCBW-0.5, CCBW-1 and CCBW-2 (figure 5 (c)) were 194, 218 and 165 F g^{-1}, respectively at 0.5 A g^{-1}. This valuable performance was still maintained at high specific current of 10 A g^{-1} as 95, 124 and 86 F g^{-1}, respectively, signifying the stability of the electrode material for SC applications whereby CCBW-1 presents higher C_s. Besides, there is a steady reduction in specific capacitance as the specific current increases suggesting good rate capability of the material. The higher performance at low specific current is influenced by the sufficient time available for the ions to diffuse into the pores of the material which allow full utilization of the available surface area. In general, the performance of CCBW-1 in figure 5 (a-d) is in agreement with the highest SSA from the BET measurements and the I_d/I_g ratios of the Raman results which prevails good contact between KOH as activating agent and CCBW material as observed.

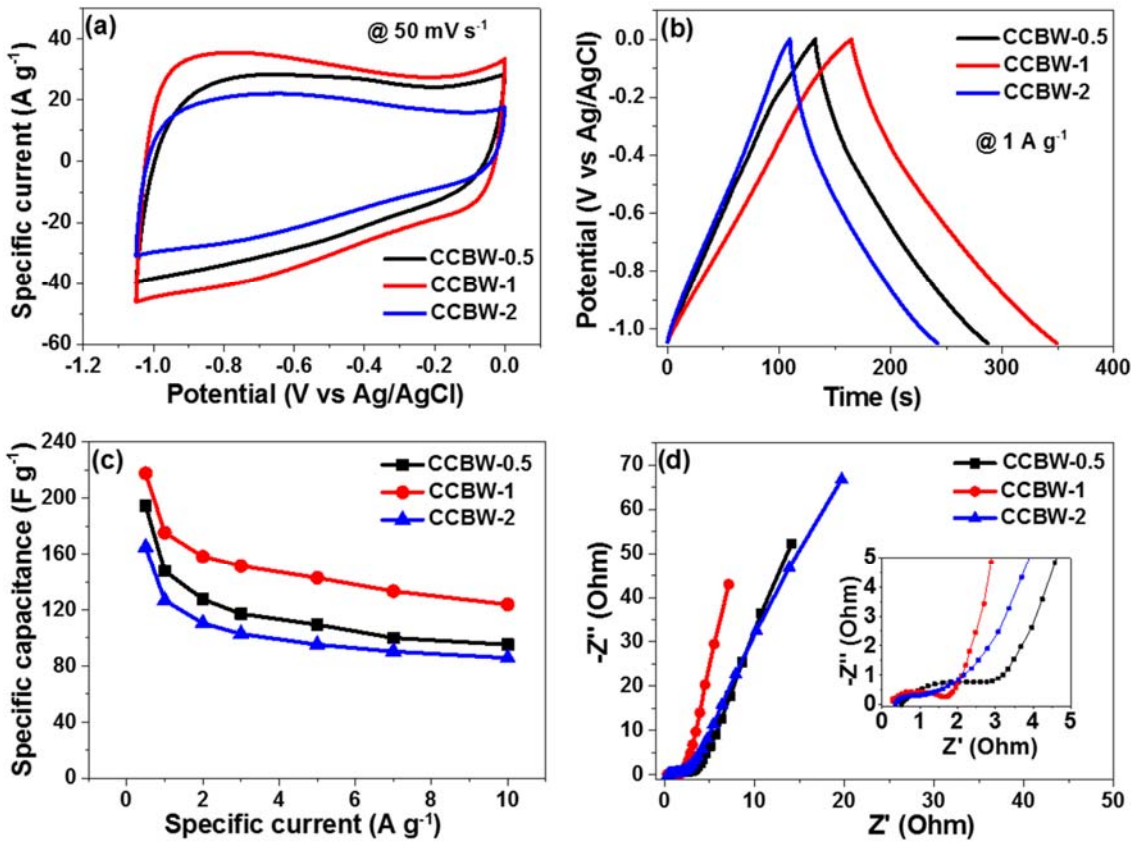

Fig. 5: Electrochemical performance in a three-electrode configuration of CCBW-0.5, CCBW-1 and CCBW-2 at 700 °C in 3 M KOH: (a) CV curves at 50 mV s^{-1} in a negative potential window, (b) GCD curves at 1 A g^{-1} in a negative potential window, (c) Specific capacitance versus specific current and (d) EIS Nyquist plot, respectively.

From the observation in figure 5 (a-d), the CCBW-1 at 700 °C was employed to fabricate the symmetric device. Despite the limitation of Faradic behaviour in the positive potential window, the symmetric device was fabricated using 3 M KOH basic aqueous electrolyte so as to study its properties. The mass balance of the positive and negative electrode in figure S2 (a) was done as shown in equation S1. Figure S2 (b-e) display the electrochemical performance of the device presenting the pseudocapacitive behaviour resulting from the synergetic effect of the positive and negative potential with a cell voltage of 1.5 V. The highest specific energy and power evaluated from the GCD curve using equation S3 were 9.1 Wh kg^{-1} and 254 W kg^{-1}, respectively at 0.5 A g^{-1}. The low charge storage (specific capacity of 18.1 mAh g^{-1} calculated

using equation S2) displayed by the device at 0.5 A g^{-1} is associated with the electrolysis of water in the KOH electrolyte which limits the cell potential and stability of the device as observed in the rate capability (figure S2 (d)), thus restricts the specific energy. Following the poor performance exhibited by the symmetric device in 3 M KOH basic aqueous electrolyte, a detailed study using neutral electrolytes was conducted on CCBW-1 at 700 °C. The stability and pH of the neutral electrolyte has an advantage of greater safety, extended potential window and wide range of operating temperature.

Figure 6 (a, b) present the rectangular CV curves at 50 mV s^{-1} which reveals EDLC behaviour for CCBW-1 using various neutral electrolytes (1 M Li_2SO_4, 1 M $NaNO_3$, 1 M Na_2SO_4 and 2.5 M KNO_3) in a positive and negative potential range of 0.0 – 0.7 V vs Ag/AgCl and -0.9 – 0.0 V vs Ag/AgCl, respectively. Both operating potential windows show that CCBW-1 corroborates higher current response in 1 M $NaNO_3$ compared to other electrolytes signifying higher specific capacitance. Further exploration was conducted to evaluate the performance of the material using GCD measurements at 1 A g^{-1}. The CCBW-1 exhibits a symmetrical triangular shape in all electrolytes as shown in figure 6 (c, d). The characteristic behaviour is in agreement with the features displayed by the CV curves in figure 6 (a, b) confirming the capacitive behaviour of the carbon material. The operating potential range (0.0-0.7 to -0.9-0.0 V vs Ag/AgCl) was maintained for all electrolytes however, longer discharge time was noticed for CCBW-1 in 1 M $NaNO_3$ compared to 1 M Li_2SO_4, 1 M Na_2SO_4 and 2.5 M KNO_3 electrolyte. Figure 6 (e, f) represent the specific capacitance (C_s) versus various specific current calculated using equation (1) for different neutral electrolytes in a positive and negative potential window. From the figures, the CCBW-1 demonstrates higher C_s in both potential windows using 1 M $NaNO_3$ compared to other electrolytes. It was also noted that the material was able to maintain 50 % of its initial C_s at higher specific current of 10 A g^{-1}.

The electrochemical impedance spectroscopy (EIS) was performed to describe the electrical resistance of the CCBW-1/electrolyte interface in a frequency range of 10 mHz – 100 kHz as shown in figure 6 (g). The intersect at x-axis (Z' axis) presents the equivalent series resistances (ESR) which are 3.3, 1.5, 2.8 and 1.6 Ω for 1 M Li_2SO_4, 1 M $NaNO_3$, 1 M Na_2SO_4 and 2.5 M KNO_3, respectively. From the figure it can be observed that the sample measured using 1 M $NaNO_3$ shows shorter diffusion length and small ESR value compared to other electrolytes. This propose that the electrode is more conductive in this particular electrolyte and hence mimics the polarization within the material.

Generally, as displayed in figure 6 (a-g) the performance of CCBW-1 in neutral electrolytes is attributed by different ions which include cation and anion sizes. Some studies have shown that the specific capacitance increases following the size of cations as $Li^+ < Na^+ < K^+$ (0.69 < 1.02 < 1.38 Å) instead of cation crystal radius $K^+ < Na^+ < Li^+$ (3.31 < 3.58 < 3.82 Å) when combined using the same anions [24,58]. This indicates that small ionic size is useful for increasing specific capacitance however similar behaviour was not shown by other studies [59]. In this study, the specific capacitance followed similar trend of $Li^+ < Na^+$ for the sulphate electrolytes while $Na^+ < K^+$ was followed for the nitrate electrolytes. For the case of anions, the following order was preserved $NO_3^- < SO_4^{2-}$ (2.64 < 2.90 Å). This shows that the behaviour of these electrolytes is contributed by the rapid ion transmission between the electrode/electrolyte interface whereby the ionic size plays an important role in a CCBW-1 material and hence the observed performance in 1 M $NaNO_3$. Furthermore, it should be noted that some material might not have the same anions and/or cations order in different neutral electrolytes due to different preparation method, morphology and structure. For example, the diffusion of electrolyte ions into the electrode material might be affected by low/high CV scan rate/GCD specific current and various preparation route which generate pores with different pore sizes. Scheme 2 illustrates the representation of cations and anions of neutral electrolyte used in this study.

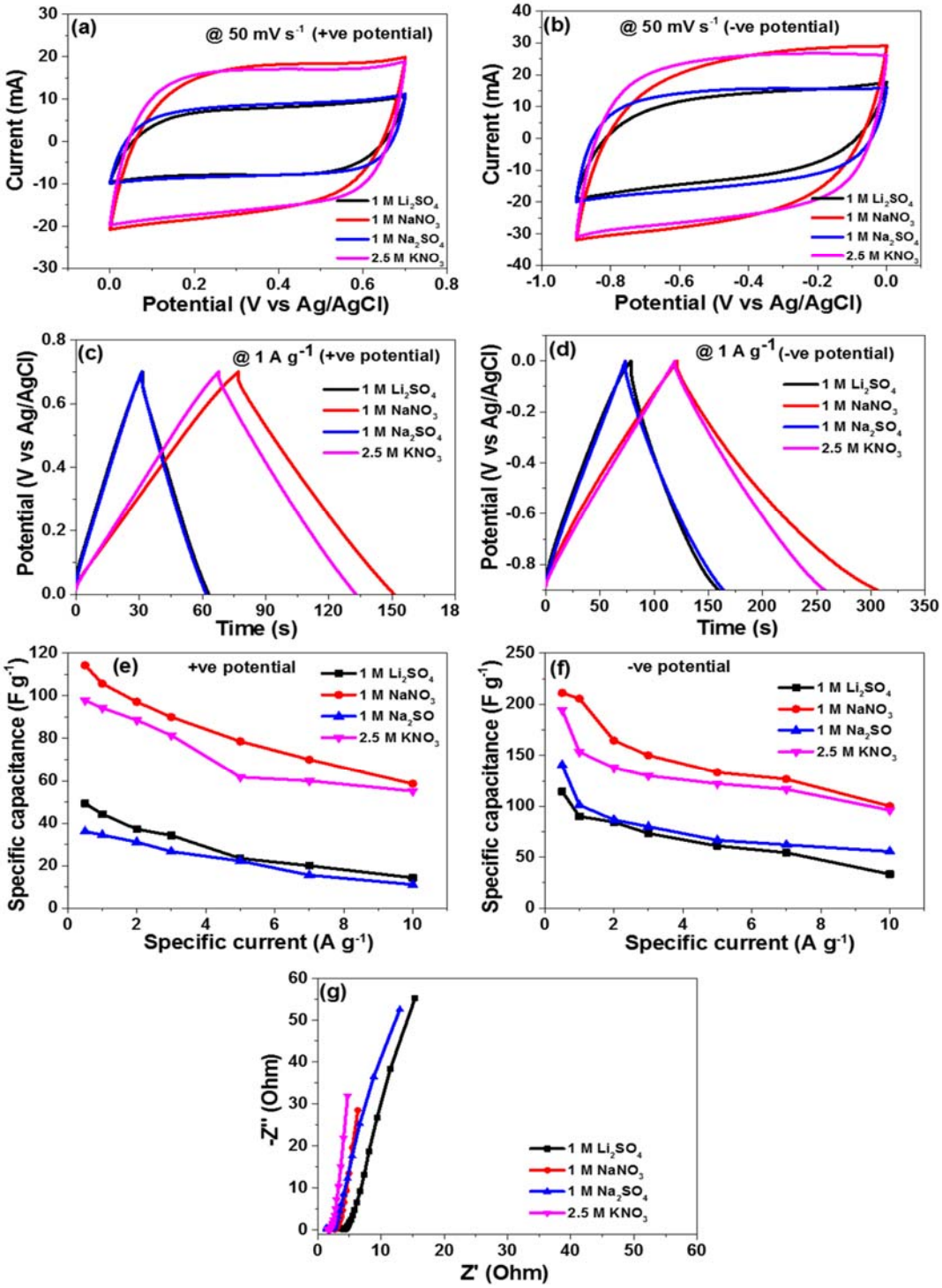

Fig. 6: (a, b) CV curves at a scan rate of 50 mVs^{-1} in both positive and negative potential windows, (c, d) GCD curves at a specific current of 1 A g^{-1} in both positive and negative potential windows, (e, f) Specific capacitance against specific current and (g) EIS Nyquist plot for CBW-1 in 1 M Li_2SO_4, 1 M $NaNO_3$, 1 M Na_2SO_4 and 2.5 M KNO_3, respectively.

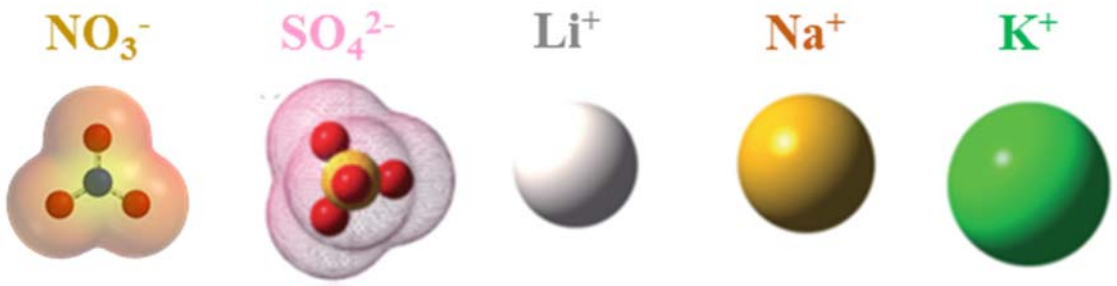

Scheme 2: Schematic representation of shape and sizes of ions (anions and cations) in neutral electrolytes [60].

In addition, the CCBW-1 was assessed by CV curves at various scan rates (5 to 100 mVs^{-1}) in a positive (0.0 - 0.7 V vs Ag/AgCl) and negative (-0.9 - 0.0 vs Ag/AgCl) potential windows as shown in figure S3 (a, b). The capacitive behaviour was maintained as the scan rate increases. However, at high scan rates there was a slight deviation from the perfect rectangular shape due to the small time taken by ions to diffuse inside the material and thus results into partial charge accumulation on the surface of the electrode. Moreover, a certain electrode and electrolyte resistance might cause the distortion of the CV curve at high scan rates. This occurs when there is a potential loss results from the current passing via the electrode and electrolyte resistance, which act as a basis for the actual potential on the electrode to be smaller than the external applied potential. Thus, the current response increases as the scan rate increases resulting into greater potential loss and therefore a smaller potential is used to initiate the ions within the electrode material. The electrode was also performed via GCD curves as presented in figure S3 (c, d) through different specific currents (0.5 to 10 A g^{-1}) and the symmetric triangular curves were observed in both potential windows which agrees with the CV curves. Sequentially, the CCBW-1 was employed as both positive and negative electrodes to fabricate the symmetric device in 1 M $NaNO_3$ electrolyte because of its best electrochemical performances as compared to other neutral electrolytes.

For the symmetric device, it is expected that the working potential will split equally between the two electrodes through the advantage of the same material utilized as the active material. However, it is not always the case as the splitting in working potential is attributed by the capacitance of the active material in each electrode. Thus, to achieve potential equivalence, mass balance of the electrode was done via charge balance of the positive and negative electrode and attained as $Q_+ = Q_-$ whereby the charge in each electrode is presented as [9]:

$$Q = C_s \times m\,\Delta V \tag{2}$$

where, Q (C) indicate charge stored on the electrode, C_S (F g^{-1}) stand for specific capacitance of the electrode based on the mass of the active material, m (g) present mass of the active material, and ΔV (V) is the potential window. For positive electrode $Q_+ = C_{s+} \times m_+\,\Delta V_+$ and negative electrode $Q_- = C_{s-} \times m_-\,\Delta V_-$. Since $Q_+ = Q_-$ then the mass balance between the positive and negative electrodes was accomplished as:

$$\frac{m_+}{m_-} = \frac{C_{s-} \times \Delta V_-}{C_{s+} \times \Delta V_+} \tag{3}$$

Thus, equation (3) was followed to balance the masses of the electrodes providing a ratio of 1.0:2.2 which resulted in total mass electrodes of 4.1 mg/cm^2.

3.4.2 Two-electrode evaluation for the symmetric device

Figure 7 (a) represents the CV curves of the symmetric device CCBW-1//CCBW-1 at different scan rates assorted from 5 to 200 mVs^{-1} using 1 M $NaNO_3$ electrolyte. The rectangular shape is exhibited by the CV curves revealing the EDLC characteristics of the carbon material. It was anticipated that, the combination of the positive and negative electrodes might provide a voltage window of 1.6 V, nonetheless our device was able to operate in an extended voltage of 1.7 V which confirms the distinctive behaviour of a neutral electrolyte. This is also contributed by lower H^+ and OH^- concentration compared to basic aqueous electrolyte (figure S2 (b)), thus

higher over-potential for hydrogen and oxygen might be anticipated. It was further observed that, the capacitive response was sustained as the scan rate increases and the shape was maintained. This reveals exceptional ion diffusion inside the pores and fast ion transport among the active material and the current collector within the symmetric device. It also indicates that the material within the device has low contact resistance thus improve its electrical conductivity.

Congruently, figure 7 (b) displays the GCD curves of the symmetric device CCBW-1//CCBW-1 at different specific current of 0.5 to 10 A g^{-1} displaying a triangular array signifying double layer capacitor. The symmetric device was able to operate in the same voltage window of 1.7 V with negligible IR drop. The specific capacitance versus specific current of the symmetric device was calculated from the GCD curves using equation (1) and presented in figure 7 (c). The maximum specific capacitance per electrode recorded for the symmetric device was 170 F g^{-1} at 0.5 A g^{-1} in which 113 F g^{-1} was sustained at high specific current of 10 A g^{-1} signifying good rate capability of the material. This confirms that even at high specific current the charge transfer between the electrode/electrolyte interfaces was maintained due to the stability of 1 M $NaNO_3$ neutral electrolyte in which the same case was not shown by 3 M KOH basic aqueous electrolyte as displayed in figure S4.

EIS measurement was performed on the CCBW-1//CCBW-1 symmetric device to investigate the internal resistance and the electrochemical behaviour of the electrode material at electrode-electrolyte interface. The experimental and fitting results are presented using Nyquist plot as shown in figure 7 (d) with an expanded view of an inset to figure 7 (di). A small semi-circle arc is observed at high frequency region which occurs due to fast charge transfer kinetics that exist at electrode/electrolyte interface. This small semicircle describes good electrical conductivity and lower resistance. A straight line closer to the y-axis was also observed at low frequency region signifying the capacitive behaviour for the device. The intersections of Z’

axis presents the equivalent series resistance (ESR) value of 0.8 Ω and its resultant charge transfer resistance (R_{CT}) evaluated from the radius of the arc as 1.9 Ω. ESR is the summation of the interface resistance of the working electrode and ions from the electrolyte, and a contact resistance between the working electrode and the current collector which used as a most important parameters to consider when evaluating materials for supercapacitor. For example, when the ESR value is high it reduces the supercapacitor performance due to high potential drop [61]. On the other hand, R_{CT} parameter indicates part of over potential which affect the specific current. Thus, the small R_{CT} is influenced by fast charge transfer kinetics which takes place at the interface of the electrodes and electrolytes. Z-fitting circuit inset d-ii to figure 7 comprises of R1, R2, Q2, W2 and C3 representing ESR, R_{CT}, constant phase element, Warburg element and mass capacitance, respectively. The ESR and R_{CT} attained from the fitted plot were 0.7 and 1.3 Ω which are equivalent to the experimental values of 0.8 and 1.9 Ω, respectively.

Bode plot presented by phase angle versus frequency curve is another technique used to evaluate the EIS data. For real application, a Bode plot is a good technique of presenting the bandwidth of a supercapacitor and its capability to work with signals that comprises of specific frequency. Normally a phase angle of -90^o, 0^o and +90^o expresses an ideal capacitor, ideal resistor and ideal inductor, respectively, while the values in between specify the non-ideal or mixed behaviour subject to the system under study [62]. For example, non-ideal behaviour can be viewed through a distorted semicircles and slanted angles in the Nyquist plot. Figure 7 (e) displays the Bode phase plot which articulates the charge storage mechanism for EDLC materials. This follows when the phase angle is close to -90^o at low frequency region, whereby, for our case the phase angle obtained was -85^o which is a good indication for double layer phenomenon.

Figure 7 (f) displays the imaginary capacitance (C''(ω)) and real capacitance (C'(ω)) against frequency curve which was obtained by using a complex capacitance model. The model is established on the single RC time-constant which explore the frequency behaviour and relaxation time constant of a carbon material. At low frequency region the device demonstrates a capacitance (C(ω)) which is a totality of C'(ω) and C''(ω) parts of capacitance as shown in the subsequent equations [61,63]:

$$C(\omega) = C'(\omega) + C''(\omega)$$

where, ω is the angular frequency ($\omega = 2\pi f$), C''(ω) present the energy dissipation of the electrode via a voltage (IR) drop and an unalterable Faradic charge transfer mechanism while C'(ω) stands for stationary capacitance attained through steady current discharge. The C'(ω) in figure 7 (f) drops steadily as the frequency escalates and a maximum peak was noticed at a frequency (f_o) of 0.34 Hz of the C''(ω). The relaxation time (τ_o) which express the lowest time required to charge the device is obtained by relating the frequency (f_o) as $\tau_o = 1/2\pi f_o$ which equals to 0.47 s in our case. This shows that the fabricated device takes a very short time of about 0.47 s to charge to the full potential which reveal an incredible behaviour of a supercapacitor that is contributed by a good electrical conductivity and fast ions transport between the electrode and electrolyte.

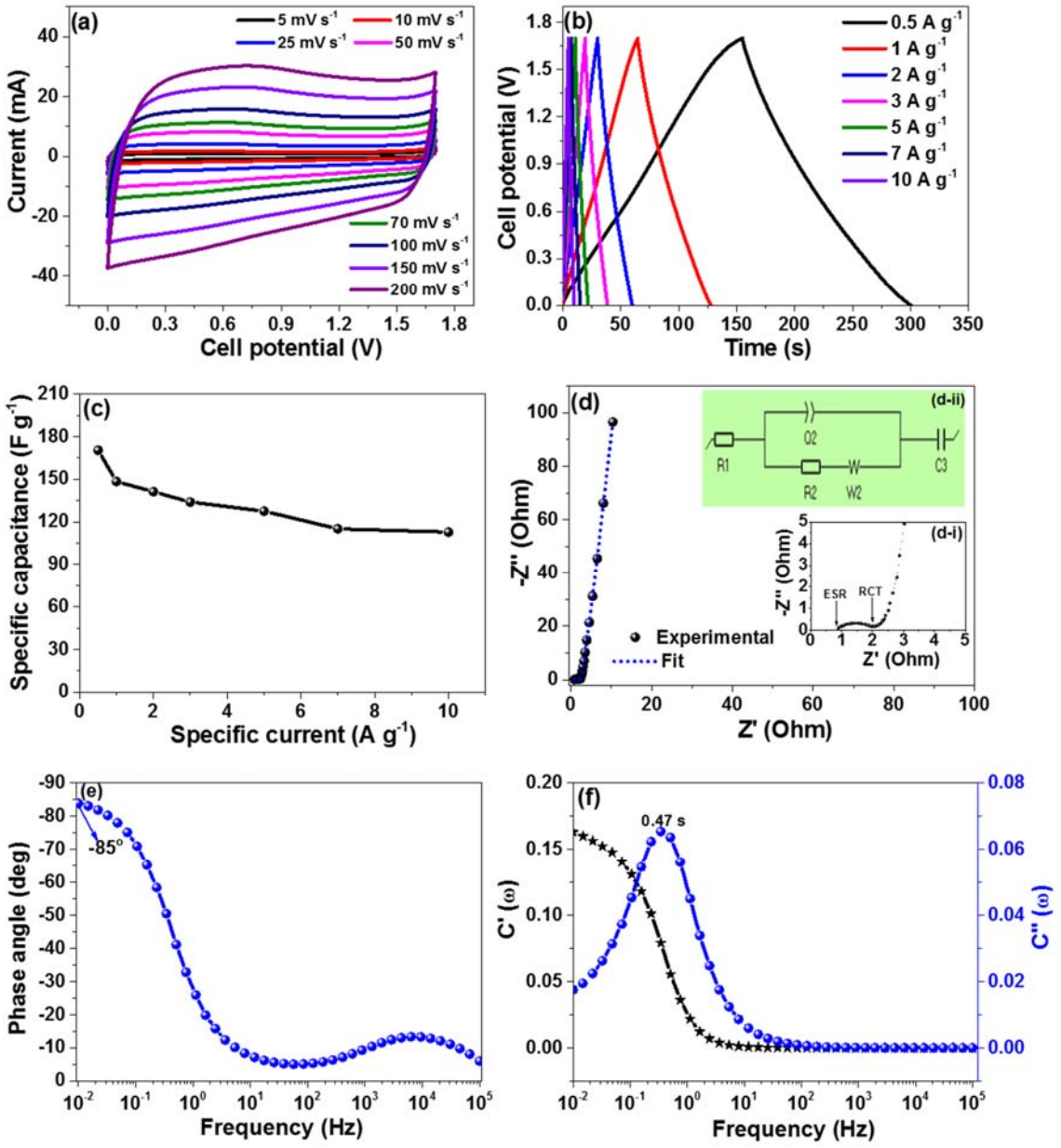

Fig. 7: Electrochemical evaluation of the symmetric device CCBW-1//CCBW-1: (a) CV curves at various scan rates, (b) GCD curves at various specific currents, (c) Specific capacitance against specific current, (d) EIS Nyquist plot with d-i and d-ii representing an insert of the magnified high frequency region and the Z-fitting circuit to the data, (e) Bode plot and (f) Capacitance C' and C'' variation as a function of frequency.

The Ragone plot demonstrating energy-power characteristics of CCBW-1//CCBW-1 symmetric device using 1 M $NaNO_3$ neutral electrolyte (blue in colour) is presented in figure

8 (a). The specific energy and power values for the symmetric device were obtained through the following expressions [9]:

$$E_d = \frac{C_s \times (\Delta V)^2}{28.8} \text{ [Wh kg}^{-1}\text{]} \quad (6)$$

$$P_d = \frac{E_d}{\Delta t} \times 3600 \text{ [W kg}^{-1}\text{]} \quad (7)$$

where, E_d and P_d present specific energy and power, respectively. The device provides the highest specific energy of 17.1 Wh kg^{-1} with its equivalent specific power of 425 W kg^{-1} at 0.5 A g^{-1}. Besides, at high specific current of 10 A g^{-1} the device was able to retain a specific energy of 11.3 Wh kg^{-1} and specific power of 8500 W kg^{-1} which shows about 66% of the initial specific energy and power was preserved. This result was compared to our fabricated CCBW-1//CCBW-1 symmetric device using 3 M KOH basic aqueous electrolyte (red in colour) and other reported studies as displayed in table 1 and figure 8 (a) where the presented symmetric device demonstrate improved values. Up to now this is the first study reporting the use of cooked chicken bone waste (CCBW) for supercapacitor applications. In the literature there are limited reports on the activated carbon from biomass waste specifically animal bones for supercapacitor applications. Thus, this study partakes a great potential and will open the door for CCBW to be used as electrode material for SC applications.

The columbic efficiency and capacitance retention as function of cycle number is displayed in figure 8 (b). Columbic efficiency (C_E) was performed to assess the charge sustainability of the CCBW-1//CCBW-1 symmetric device and it was calculated using the following equation [15]:

$$C_E = \frac{t_D}{t_c} \times 100\% \quad (10)$$

Where t_c and t_D are charging and discharging times with the same specific current respectively. The device was charged and discharged at 5 A g^{-1} for 20,000 cycling and presented a columbic

efficiency of 99.8% which is close to 100%. Also, it was verified that the device was able to retain about 90.1% of its initial capacitance at the same specific current. Usually, for an ideal supercapacitor the columbic efficiency is 100% however practically, supercapacitor performance is limited by conductivity and decomposition of water in the electrolyte which results into oxygen evolution reaction (OER) and hydrogen evolution reaction (HER). On the other hand, in this study it was observed that there is an increase in the quantity of electroactive sites through prolonged charge-discharge whereby fundamentally they are accountable for fast charge transfer kinetics and hence the observed performance. The results obtained reveals that our device is performing close to the ideal supercapacitor.

Further evaluation on the suitability of the device was done via a voltage holding as exhibited in figure 8 (c). Herein, the device was charged-discharged for three cycles to a maximum potential of 1.7 V at 5 A g^{-1} and then held at that potential for 10 h while monitoring its specific capacitance. It was observed that there was an increase in specific capacitance from 127.6 F g^{-1} to 329.41 F g^{-1} after 300 h. This correspond to the specific energy of 33.1 Wh kg^{-1} and specific power of 4,250 W kg^{-1} at 5 A g^{-1} after 300 h. It can be observed that, at the beginning of the electrochemical process the electrode/electrolyte interaction might be weak due to lack of wettability to the electrode's pores at the initial stage. Thus, after long cycling (voltage holding) there is an improvement in performance as presented in figure 8 (d) displaying the CV curves of the device shown an increase in current response after voltage holding compared to before cycling and after cycling stability. This performance is expected to be contributed by the ease access of the electrolyte ions in the concealed pores within the material which facilitate wettability and contact among the electrolyte ions and the surface of the material. This also initiated the decrease in internal resistance in which an improvement in diffusion length for the EIS Nyquist plot is observed in figure 8 (e) revealing appropriate wettability within the material. The practical evaluation of the fabricated CCBW-1//CCBW-1 symmetric device was

done through lighting 3 V red light-emitting diode (LED). The process of illumination was done by connecting two coin cells in series as displayed in figure 8 (f). The outcome proposes that the fabricated symmetric device will add value in the energy storage industry thus can be used in different portable electronic devices. Figure 8 (g, h) display SEM morphology at low and high magnification for the device after voltage holding. The images confirm insignificant variation in morphology as compared to figure 1 (d, e) which indicates higher structural stability of the electrode materials.

Table 1: Assessments of electrochemical performance of various biomass from the literature with similar material evaluated in two-electrode system.

Biomass material	**Specific surface area (m^2/g)**	**Electrolyte**	**Specific energy ($Wh\ kg^{-1}$)**	**Specific power ($W\ kg^{-1}$)**	**Cycling stability**	**Ref.**
Pork bone	1260	6 M KOH	6.5	300	**-**	[53]
Feather finger grass flower (FFGF)	637.1	1MEt4NBF4 /AN	13.18	610	10,000 ($10\ A\ g^{-1}$)	[22]
Mango kernels	-	1 M H_2SO_4	11.8	666	5000 ($100\ mV\ s^{-1}$)	[63]
Blackfish bone	1202	6 M KOH	7.0	300	-	[53]
Carchorus Olitorius (Jute Fiber)	1903	6 M KOH	15.44	403	10,000 ($2\ A\ g^{-1}$)	[50]
Commercial carbon (YP- 80F)	1683.4	2.5 M KNO_3	13.1	461.2	10,000 ($3\ A\ g^{-1}$)	[59]
Camellia oleifera	1726	2 M H_2SO_4	9.55	478	10,000 ($10\ A\ g^{-1}$)	[19]
Eel bone	1163	6 M KOH	6.8	300	-	[53]
AC from Al-MOF	1100.9	KOH/PVA	6.77	100	10,000 ($10\ A\ g^{-1}$)	[64]
Cooked chicken bone waste	2235.8	**3 M KOH**	**9.1**	**254**	**-**	**This work (a)**
		1 M $NaNO_3$	**17.1**	**425**	**20,000 ($5\ A\ g^{-1}$)**	**This work (b)**
			33.1	**4250**	**300 h floating time**	**This work**

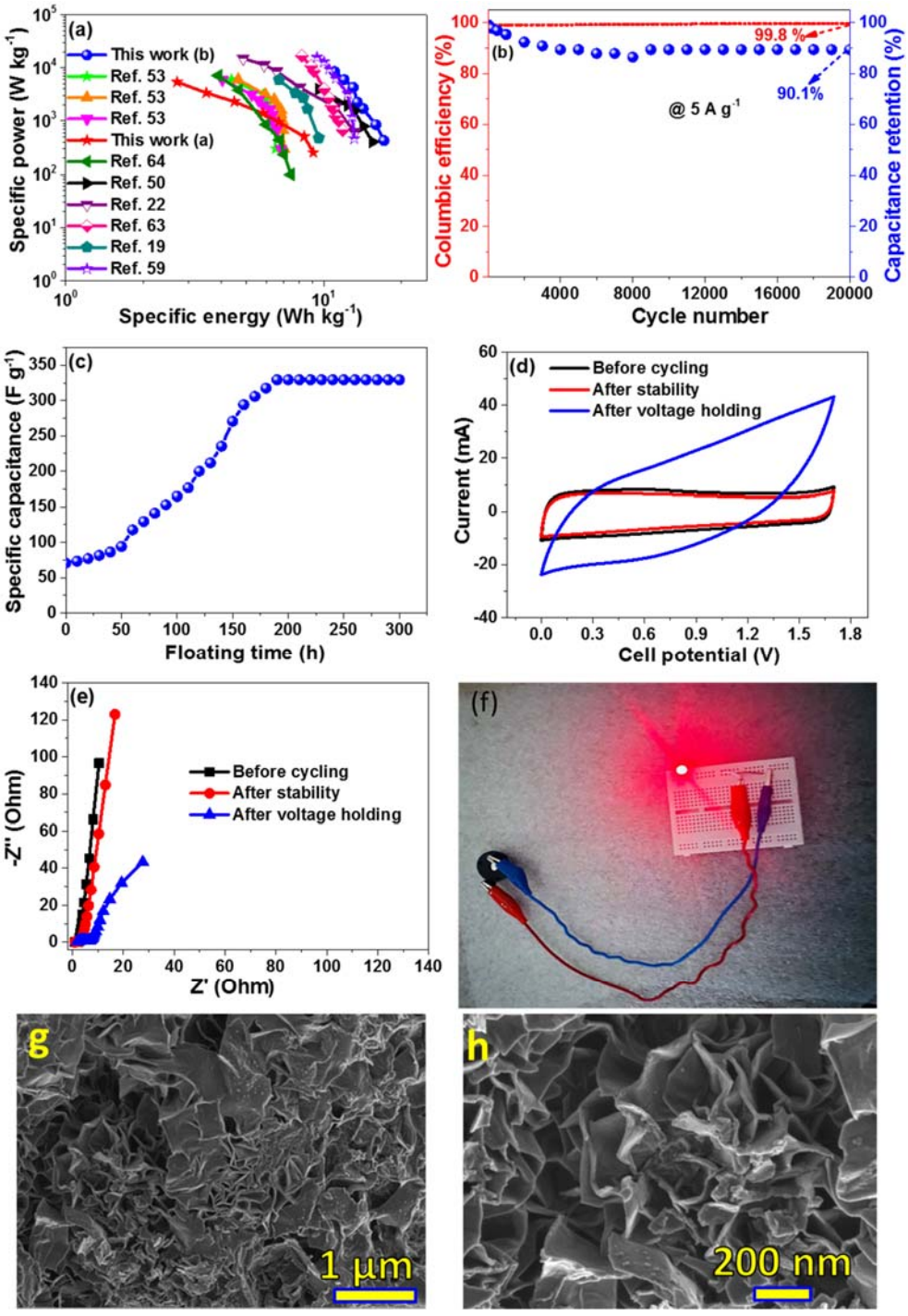

Fig. 8: (a) Ragone plot of the CCBW-1//CCBW-1 symmetric device, (b) Columbic efficiency and capacitance retention versus cycle number, (c) Specific capacitance versus floating time (d) CV curves before cycling, after cycling stability and after voltage holding at 50 mV s^{-1}, (e) EIS Nyquist plot before cycling, after cycling stability and after voltage holding, (f) Digital image of two devices connected in series used to illuminate 3 V LED bulb and (g, h) SEM images at low and high magnification after voltage holding.

4. CONCLUSION

The promising porous carbon material from cooked chicken bone waste (CCBW) was successfully produced and reported for the first time as electrode material for supercapacitor devices. This assertion is confirmed by different characterization techniques and electrochemical analysis. The material (CCBW-1) was tested in a three-electrode setup using 3 M KOH basic aqueous electrolyte and presented a capacitance of 218 F g^{-1} at 0.5 A g^{-1} in a negative potential window of 1.05 V vs Ag/AgCl. The positive potential window presented the Faradic behavior hence limit the properties of capacitive behavior in the overall device. Further evaluation was done using 1 M Li_2SO_4, 1 M $NaNO_3$, 1 M Na_2SO_4 and 2.5 M KNO_3 neutral electrolytes in a three-electrode configuration. It was observed that 1 M $NaNO_3$ electrolyte out performed all other neutral electrolytes through a potential range of 0.0-0.7 to -0.9-0.0 V vs Ag/AgCl displaying a maximum capacitance of 114 and 211 F g^{-1} at 0.5 A g^{-1} in a positive and negative potential window, respectively and hence it was further used for evaluation of the symmetric device. The CCBW-1//CCBW-1 symmetric device was successfully produced in a two-electrode setup and revealed the highest specific energy and power of 17.1 Wh kg^{-1} and 425 W kg^{-1} at 0.5 A g^{-1}, which are higher than 9.07 Wh kg^{-1} and 254 W kg^{-1} obtained using 3 M KOH electrolyte. Besides, at high specific current of 10 A g^{-1} the device was able to maintain a specific energy and power of 11.3 Wh kg^{-1} and 8500 W kg^{-1} which indicates almost 66% of the initial specific energy and power was conserved. The device demonstrated exceptional columbic efficiency of 99.8% and capacitance retention of 90.1% after 20,000 cycling at 5 A g^{-1}. Moreover, there was an increase in specific capacitance per electrode from 127.6 F g^{-1} to 329.41 F g^{-1} after 300 h. This correspond to the specific energy of 33.1 Wh kg^{-1} and specific power of 4,250 W kg^{-1} at 5 A g^{-1} after 300 h of the voltage holding. Therefore, the use of CCBW as a positive and negative electrode is vital for scale up and cost-effectiveness. Hence, CCBW reserves as a sustainable and renewable waste for commercial supercapacitor application.

ACKNOWLEDGEMENTS

We sincerely acknowledge research support from South African Research Chairs Initiative of the Department of Science and Technology and National Research Foundation of South Africa (Grant No. 61056). Any opinion, finding, and conclusion expressed in this material are that of the authors, and the NRF does not accept any liability in this regard. Delvina Japhet Tarimo acknowledges the financial support from NRF through SARChI chair in Carbon Technology and Materials.

REFERENCES

[1] J.R. Rajabathar, M. Sivachidambaram, J.J. Vijaya, H.A. Al-Lohedan, D.M.D. Aldhayan, Flexible Type symmetric supercapacitor electrode fabrication using phosphoric Acid-activated carbon nanomaterials derived from cow dung for renewable energy applications, ACS Omega. 5 (2020) 15028–15038. https://doi.org/10.1021/acsomega.0c00848.

[2] Y. Zhou, J. Ren, L. Xia, Q. Zheng, J. Liao, E. Long, F. Xie, C. Xu, D. Lin, Waste soybean dreg-derived N/O co-doped hierarchical porous carbon for high performance supercapacitor, Electrochim. Acta. 284 (2018) 336–345. https://doi.org/10.1016/J.ELECTACTA.2018.07.134.

[3] A. Bello, N. Manyala, F. Barzegar, A.A. Khaleed, D.Y. Momodu, J.K. Dangbegnon, Renewable pine cone biomass derived carbon materials for supercapacitor application, RSC Adv. 6 (2016) 1800–1809. https://doi.org/10.1039/c5ra21708c.

[4] K.M. Rambau, D.J. Tarimo, O. Fasakin, N.M. Musyoka, N. Manyala, Asymmetric supercapacitor based on novel coal fly ash derived metal–organic frameworks as

positive electrode and its derived carbon as negative electrode, J. Appl. Electrochem. (2022). https://doi.org/10.1007/s10800-022-01672-3.

[5] N.A. Cano, J.O. Velasco, I.B. Franco, Science for Sustainable Societies Actioning the Global Goals for Local Impact, 2020. https://doi.org/10.1007/978-981-32-9927-6.

[6] S. Chu, Y. Cui, N. Liu, The path towards sustainable energy, Nat. Mater. 16 (2016) 16–22. https://doi.org/10.1038/nmat4834.

[7] Q. Pan, D. Gong, Y. Tang, Recent progress and perspective on electrolytes for sodium/potassium-based devices, Energy Storage Mater. 31 (2020) 328–343. https://doi.org/10.1016/j.ensm.2020.06.025.

[8] S. Maddukuri, D. Malka, M.S. Chae, Y. Elias, S. Luski, D. Aurbach, On the challenge of large energy storage by electrochemical devices, Electrochim. Acta. 354 (2020) 136771. https://doi.org/10.1016/J.ELECTACTA.2020.136771.

[9] D.J. Tarimo, K.O. Oyedotun, A.A. Mirghni, N.F. Sylla, N. Manyala, High energy and excellent stability asymmetric supercapacitor derived from sulphur-reduced graphene oxide/manganese dioxide composite and activated carbon from peanut shell, Electrochim. Acta. 353 (2020) 136498. https://doi.org/10.1016/j.electacta.2020.136498.

[10] M. Winter, R.J. Brodd, What are batteries, fuel cells, and supercapacitors?, Chem. Rev. 104 (2004) 4245–4269. https://doi.org/10.1021/cr020730k.

[11] A.R. Dehghani-Sanij, E. Tharumalingam, M.B. Dusseault, R. Fraser, Study of energy storage systems and environmental challenges of batteries, Renew. Sustain. Energy Rev. 104 (2019) 192–208. https://doi.org/10.1016/j.rser.2019.01.023.

[12] K.O. Oyedotun, M.J. Madito, D.Y. Momodu, A.A. Mirghni, T.M. Masikhwa, N. Manyala, Synthesis of ternary NiCo-MnO2 nanocomposite and its application as a novel high energy supercapattery device, Chem. Eng. J. 335 (2018) 416–433. https://doi.org/10.1016/j.cej.2017.10.169.

[13] P. Dubey, V. Shrivastav, P.H. Maheshwari, S. Sundriyal, Recent advances in biomass derived activated carbon electrodes for hybrid electrochemical capacitor applications: Challenges and opportunities, Carbon N. Y. 170 (2020) 1–29. https://doi.org/10.1016/J.CARBON.2020.07.056.

[14] M.Z. Iqbal, U. Aziz, Supercapattery: Merging of battery-supercapacitor electrodes for hybrid energy storage devices, J. Energy Storage. 46 (2022) 103823. https://doi.org/10.1016/J.EST.2021.103823.

[15] D.J. Tarimo, K.O. Oyedotun, A.A. Mirghni, N. Manyala, Sulphur-reduced graphene oxide composite with improved electrochemical performance for supercapacitor applications, Int. J. Hydrogen Energy. 45 (2020) 13189–13201. https://doi.org/10.1016/j.ijhydene.2020.03.059.

[16] P.A. Goodman, H. Li, Y. Gao, Y.F. Lu, J.D. Stenger-Smith, J. Redepenning, Preparation and characterization of high surface area, high porosity carbon monoliths from pyrolyzed bovine bone and their performance as supercapacitor electrodes, Carbon N. Y. 55 (2013) 291–298. https://doi.org/10.1016/j.carbon.2012.12.066.

[17] Y.L. Zhang, C. Sun, Z.S. Tang, High specific capacitance and high energy density supercapacitor electrodes enabled by porous carbon with multilevel pores and self-doped heteroatoms derived from Chinese date, Diam. Relat. Mater. 97 (2019) 107455. https://doi.org/10.1016/J.DIAMOND.2019.107455.

[18] R.A. Senthil, S. Osman, J. Pan, X. Liu, Y. Wu, Recent progress on porous carbon derived from Zn and Al based metal-organic frameworks as advanced materials for supercapacitor applications, J. Energy Storage. 44 (2021) 103263. https://doi.org/10.1016/j.est.2021.103263.

[19] X. Bo, K. Xiang, Y. Zhang, Y. Shen, S. Chen, Y. Wang, M. Xie, X. Guo, Microwave-assisted conversion of biomass wastes to pseudocapacitive mesoporous carbon for high-

performance supercapacitor, J. Energy Chem. 39 (2019) 1–7. https://doi.org/10.1016/j.jechem.2019.01.006.

[20] F. Béguin, V. Presser, A. Balducci, E. Frackowiak, Carbons and electrolytes for advanced supercapacitors, Adv. Mater. 26 (2014) 2219–2251. https://doi.org/10.1002/adma.201304137.

[21] J. Zhang, L. Jin, J. Cheng, H. Hu, Hierarchical porous carbons prepared from direct coal liquefaction residue and coal for supercapacitor electrodes, Carbon N. Y. 55 (2013) 221–232. https://doi.org/10.1016/J.CARBON.2012.12.030.

[22] R.A. Senthil, V. Yang, J. Pan, Y. Sun, A green and economical approach to derive biomass porous carbon from freely available feather finger grass flower for advanced symmetric supercapacitors, J. Energy Storage. 35 (2021) 102287. https://doi.org/10.1016/j.est.2021.102287.

[23] N.F. Sylla, N.M. Ndiaye, B.D. Ngom, B.K. Mutuma, D. Momodu, M. Chaker, N. Manyala, Ex-situ nitrogen-doped porous carbons as electrode materials for high performance supercapacitor, J. Colloid Interface Sci. 569 (2020) 332–345. https://doi.org/10.1016/J.JCIS.2020.02.061.

[24] B. Pal, S. Yang, S. Ramesh, V. Thangadurai, R. Jose, Electrolyte selection for supercapacitive devices: A critical review, Nanoscale Adv. 1 (2019) 3807–3835. https://doi.org/10.1039/c9na00374f.

[25] W. Wei, Z. Chen, Y. Zhang, J. Chen, L. Wan, C. Du, M. Xie, X. Guo, Full-faradaic-active nitrogen species doping enables high-energy-density carbon-based supercapacitor, J. Energy Chem. 48 (2020) 277–284. https://doi.org/10.1016/j.jechem.2020.02.011.

[26] K.O. Oyedotun, A.A. Mirghni, O. Fasakin, D.J. Tarimo, B.A. Mahmoud, N. Manyala, Effect of growth-time on electrochemical performance of birnessite manganese oxide

(δ-MnO2) as electrodes for supercapacitors: An insight into neutral aqueous electrolytes, J. Energy Storage. 36 (2021) 102419. https://doi.org/10.1016/J.EST.2021.102419.

[27] N. Liu, L. Chai, R.A. Senthil, W. Li, M. Krishnamoorthy, Y. Sun, X. Liu, J. Qian, X. Li, J. Pan, Couple of Nonpolarized/Polarized Electrodes Building a New Universal Electrochemical Energy Storage System with an Impressive Energy Density, ACS Appl. Mater. Interfaces. 13 (2021) 45375–45384. https://doi.org/10.1021/acsami.1c10043.

[28] V. Yang, R. Arumugam Senthil, J. Pan, T. Rajesh Kumar, Y. Sun, X. Liu, Hierarchical porous carbon derived from jujube fruits as sustainable and ultrahigh capacitance material for advanced supercapacitors, J. Colloid Interface Sci. 579 (2020) 347–356. https://doi.org/10.1016/j.jcis.2020.06.080.

[29] A. González, E. Goikolea, J.A. Barrena, R. Mysyk, Review on supercapacitors: Technologies and materials, Renew. Sustain. Energy Rev. 58 (2016) 1189–1206. https://doi.org/10.1016/j.rser.2015.12.249.

[30] G. Wang, L. Zhang, J. Zhang, A review of electrode materials for electrochemical supercapacitors, Chem. Soc. Rev. 41 (2012) 797–828. https://doi.org/10.1039/C1CS15060J.

[31] R. Liu, A. Zhou, X. Zhang, J. Mu, H. Che, Y. Wang, T.T. Wang, Z. Zhang, Z. Kou, Fundamentals, advances and challenges of transition metal compounds-based supercapacitors, Chem. Eng. J. 412 (2021) 128611. https://doi.org/10.1016/J.CEJ.2021.128611.

[32] Q. Meng, K. Cai, Y. Chen, L. Chen, Research progress on conducting polymer based supercapacitor electrode materials, Nano Energy. 36 (2017) 268–285. https://doi.org/10.1016/J.NANOEN.2017.04.040.

[33] M. Xie, Z. Xu, S. Duan, Z. Tian, Y. Zhang, K. Xiang, M. Lin, X. Guo, W. Ding, Facile growth of homogeneous Ni(OH)2 coating on carbon nanosheets for high-performance

asymmetric supercapacitor applications, Nano Res. 11 (2018) 216–224. https://doi.org/10.1007/s12274-017-1621-4.

[34] M. Xie, S. Duan, Y. Shen, K. Fang, Y. Wang, M. Lin, X. Guo, In-Situ-Grown Mg(OH)2-Derived Hybrid α-Ni(OH)2 for Highly Stable Supercapacitor, ACS Energy Lett. 1 (2016) 814–819. https://doi.org/10.1021/acsenergylett.6b00258.

[35] X. Wang, H. Song, S. Ma, M. Li, G. He, M. Xie, X. Guo, Template ion-exchange synthesis of Co-Ni composite hydroxides nanosheets for supercapacitor with unprecedented rate capability, Chem. Eng. J. 432 (2022) 134319. https://doi.org/10.1016/j.cej.2021.134319.

[36] A.R. Selvaraj, A. Muthusamy, Inho-Cho, H.J. Kim, K. Senthil, K. Prabakar, Ultrahigh surface area biomass derived 3D hierarchical porous carbon nanosheet electrodes for high energy density supercapacitors, Carbon N. Y. 174 (2021) 463–474. https://doi.org/10.1016/J.CARBON.2020.12.052.

[37] M.A. Azam, N.S.N. Ramli, N.A.N.M. Nor, T.I.T. Nawi, Recent advances in biomass-derived carbon, mesoporous materials, and transition metal nitrides as new electrode materials for supercapacitor: A short review, Int. J. Energy Res. 45 (2021) 8335–8346. https://doi.org/10.1002/er.6377.

[38] M. Kigozi, R. Kali, A. Bello, B. Padya, G.M. Kalu-Uka, J. Wasswa, P.K. Jain, P.A. Onwualu, N.Y. Dzade, Modified activation process for supercapacitor electrode materials from african maize cob, Materials (Basel). 13 (2020) 1–20. https://doi.org/10.3390/ma13235412.

[39] Z. Li, D. Guo, Y. Liu, H. Wang, L. Wang, Recent advances and challenges in biomass-derived porous carbon nanomaterials for supercapacitors, Chem. Eng. J. 397 (2020) 125418. https://doi.org/10.1016/J.CEJ.2020.125418.

[40] Z. Bi, Q. Kong, Y. Cao, G. Sun, F. Su, X. Wei, X. Li, A. Ahmad, L. Xie, C.M. Chen,

Biomass-derived porous carbon materials with different dimensions for supercapacitor electrodes: A review, J. Mater. Chem. A. 7 (2019) 16028–16045. https://doi.org/10.1039/c9ta04436a.

[41] A.K. Tripathi, S. Murugavel, R.K. Singh, Dead Ashoka (Saraca asoca) leaves–derived porous activated carbons and flexible iongel polymer electrolyte for high-energy-density electric double-layer capacitors, Mater. Today Sustain. 11–12 (2021) 100062. https://doi.org/10.1016/j.mtsust.2021.100062.

[42] M.A. Yahya, M.H. Mansor, W.A.A.W. Zolkarnaini, N.S. Rusli, A. Aminuddin, K. Mohamad, F.A.M. Sabhan, A.A.A. Atik, L.N. Ozair, A brief review on activated carbon derived from agriculture by-product, AIP Conf. Proc. 1972 (2018). https://doi.org/10.1063/1.5041244.

[43] J.P. Jyothibasu, R.H. Lee, Facile, scalable, eco-friendly fabrication of high-performance flexible all-solid-state supercapacitors, Polymers (Basel). 10 (2018) 6–8. https://doi.org/10.3390/polym10111247.

[44] K.Ö. Köse, B. Pişkin, M.K. Aydınol, Chemical and structural optimization of ZnCl2 activated carbons via high temperature CO2 treatment for EDLC applications, Int. J. Hydrogen Energy. 43 (2018) 18607–18616. https://doi.org/10.1016/J.IJHYDENE.2018.03.222.

[45] Y. Liu, J. Chen, B. Cui, P. Yin, C. Zhang, Design and Preparation of Biomass-Derived Carbon Materials for Supercapacitors: A Review, C. 4 (2018) 53. https://doi.org/10.3390/c4040053.

[46] G. Jiang, R.A. Senthil, Y. Sun, T.R. Kumar, J. Pan, Recent progress on porous carbon and its derivatives from plants as advanced electrode materials for supercapacitors, J. Power Sources. 520 (2022) 230886. https://doi.org/10.1016/j.jpowsour.2021.230886.

[47] R. Thangavel, A.G. Kannan, R. Ponraj, V. Thangavel, D.W. Kim, Y.S. Lee, High-energy

green supercapacitor driven by ionic liquid electrolytes as an ultra-high stable next-generation energy storage device, J. Power Sources. 383 (2018) 102–109. https://doi.org/10.1016/J.JPOWSOUR.2018.02.037.

[48] L. Wei, G. Yushin, Nanostructured activated carbons from natural precursors for electrical double layer capacitors, Nano Energy. 1 (2012) 552–565. https://doi.org/10.1016/J.NANOEN.2012.05.002.

[49] J. Wang, S. Kaskel, KOH activation of carbon-based materials for energy storage, J. Mater. Chem. 22 (2012) 23710–23725. https://doi.org/10.1039/c2jm34066f.

[50] P. Manasa, Z.J. Lei, F. Ran, Biomass Waste Derived Low Cost Activated Carbon from Carchorus Olitorius (Jute Fiber) as Sustainable and Novel Electrode Material, J. Energy Storage. 30 (2020) 101494. https://doi.org/10.1016/J.EST.2020.101494.

[51] K.O. Oyedotun, F. Barzegar, A.A. Mirghni, A.A. Khaleed, T.M. Masikhwa, N. Manyala, Examination of High-Porosity Activated Carbon Obtained from Dehydration of White Sugar for Electrochemical Capacitor Applications, ACS Sustain. Chem. Eng. 7 (2019) 537–546. https://doi.org/10.1021/acssuschemeng.8b04080.

[52] W. Huang, H. Zhang, Y. Huang, W. Wang, S. Wei, Hierarchical porous carbon obtained from animal bone and evaluation in electric double-layer capacitors, Carbon N. Y. 49 (2011) 838–843. https://doi.org/10.1016/j.carbon.2010.10.025.

[53] L. Niu, C. Shen, L. Yan, J. Zhang, Y. Lin, Y. Gong, C. Li, C.Q. Sun, S. Xu, Waste bones derived nitrogen–doped carbon with high micropore ratio towards supercapacitor applications, J. Colloid Interface Sci. 547 (2019) 92–101. https://doi.org/10.1016/J.JCIS.2019.03.097.

[54] M.A. Lillo-Ródenas, J. Juan-Juan, D. Cazorla-Amorós, A. Linares-Solano, About reactions occurring during chemical activation with hydroxides, Carbon N. Y. 42 (2004) 1371–1375. https://doi.org/10.1016/j.carbon.2004.01.008.

[55] J. Niu, R. Shao, J. Liang, M. Dou, Z. Li, Y. Huang, F. Wang, Biomass-derived mesopore-dominant porous carbons with large specific surface area and high defect density as high performance electrode materials for Li-ion batteries and supercapacitors, Nano Energy. 36 (2017) 322–330. https://doi.org/10.1016/J.NANOEN.2017.04.042.

[56] A. Sadezky, H. Muckenhuber, H. Grothe, R. Niessner, U. Pöschl, Raman microspectroscopy of soot and related carbonaceous materials: Spectral analysis and structural information, Carbon N. Y. 43 (2005) 1731–1742. https://doi.org/10.1016/J.CARBON.2005.02.018.

[57] N.M. Keppetipola, M. Dissanayake, P. Dissanayake, B. Karunarathne, M.A. Dourges, D. Talaga, L. Servant, C. Olivier, T. Toupance, S. Uchida, K. Tennakone, G.R.A. Kumara, L. Cojocaru, Graphite-type activated carbon from coconut shell: a natural source for eco-friendly non-volatile storage devices, RSC Adv. 11 (2021) 2854–2865. https://doi.org/10.1039/d0ra09182k.

[58] J.H. Chae, G.Z. Chen, Influences of ions and temperature on performance of carbon nano-particulates in supercapacitors with neutral aqueous electrolytes, Particuology. 15 (2014) 9–17. https://doi.org/10.1016/j.partic.2013.02.008.

[59] D. Chen, Z. Li, J. Jiang, J. Wu, N. Shu, X. Zhang, Influence of electrolyte ions on rechargeable supercapacitor for high value-added conversion of low-grade waste heat, J. Power Sources. 465 (2020) 228263. https://doi.org/10.1016/j.jpowsour.2020.228263.

[60] K. Fic, G. Lota, M. Meller, E. Frackowiak, Novel insight into neutral medium as electrolyte for high-voltage supercapacitors, Energy Environ. Sci. 5 (2012) 5842–5850. https://doi.org/10.1039/c1ee02262h.

[61] C. Portet, G. Yushin, Y. Gogotsi, Electrochemical performance of carbon onions, nanodiamonds, carbon black and multiwalled nanotubes in electrical double layer capacitors, Carbon N. Y. 45 (2007) 2511–2518.

https://doi.org/10.1016/J.CARBON.2007.08.024.

[62] J.S. Ko, C.H. Lai, J.W. Long, D.R. Rolison, B. Dunn, J. Nelson Weker, Differentiating Double-Layer, Psuedocapacitance, and Battery-like Mechanisms by Analyzing Impedance Measurements in Three Dimensions, ACS Appl. Mater. Interfaces. 12 (2020) 14071–14078. https://doi.org/10.1021/acsami.0c02020.

[63] D. Jain, J. Kanungo, S.K. Tripathi, Performance enhancement approach for supercapacitor by using mango kernels derived activated carbon electrode with p-hydroxyaniline based redox additive electrolyte, Mater. Chem. Phys. 229 (2019) 66–77. https://doi.org/10.1016/J.MATCHEMPHYS.2019.02.060.

[64] L. Fang, Y. Xie, Y. Wang, Z. Zhang, P. Liu, N. Cheng, J. Liu, Y. Tu, H. Zhao, J. Zhang, Facile synthesis of hierarchical porous carbon nanorods for supercapacitors application, Appl. Surf. Sci. 464 (2019) 479–487. https://doi.org/10.1016/j.apsusc.2018.09.124.